Gómez-Hernández, J., González-Gómez, P., Briongos, J. & Santana, D. (2020). Technical feasibility analysis of a linear particle solar receiver. *Solar Energy, 195*, pp. 102–113.

DOI: 10.1016/j.solener.2019.11.052

Technical feasibility analysis of a Linear Particle Solar Receiver

*Gómez-Hernández, J., González-Gómez, P.A., Briongos, J.V., Santana, D.

Universidad Carlos III de Madrid. Escuela Politécnica Superior. Departamento de Ingeniería Térmica y de Fluidos, Avenida de la Universidad 30, 28911, Leganés (Madrid)

*Correspondence to the author, e-mail: jegomez@ing.uc3m.es

Abstract

This work proposes a new particle receiver for Concentrating Solar Technology (CST) that employs air and particles as heat transfer fluid (HTF). The novel Linear Particle Solar Receiver (LPSR) is located at the ground level receiving the concentrated solar energy linearly from the top. This receiver is formed by several fluidized beds connected consecutively allowing the horizontal movement of solids and the linear absorption of solar energy. A new solar field is proposed and analyzed to redirect the concentrated solar energy towards the receiver linearly.

The optic analysis of a linear beam-down system is carried out using a ray-tracing software. Then, the performance of a linear particle solar receiver is analyzed considering target temperatures of 200 ºC, 400 ºC, 600 ºC and 800 ºC to reproduce CST integration with medium and high temperature process heat, Rankine power generation and supercritical CO_2 (sCO_2) cycles, respectively. The temperature of the hot streams of air and sand are calculated considering the heat losses from the receiver and the compressor parasitic consumption. The procedure to determine the optimum design is shown studying one line as a function of the target temperature. For instance, a sand mass flow of 1.75 kg/s in a receiver of 0.5 m width and a secondary reflector eccentricity of 0.8, can be heated up to 600 ºC in a length of 280 m, showing a solar field efficiency of 40.25 % and a receiver thermal efficiency of 80%.

keywords:

Concentrating Solar Technology, Linear Particle Solar Receiver, Beam-Down Linear Fresnel Reflector, Solar Energy, Fluidized Bed Technology

Nomenclature

Abbreviations

BDLFR beam-down linear Fresnel Reflector

CPCs compound parabolic concentrators

CSP concentrating solar power

CST concentrating solar technology

HTF heat transfer fluid

LFR linear Fresnel reflectors

LPSR linear particle solar receiver

sCO_2 supercritical-CO_2 cycle

Symbols

39	a	semimajor axis (m)
40	a_B	bubbles fraction (-)
41	a_p	specific surface of particles (m^{-1})
42	A_{SF}	solar field aperture area (m^2)
43	A_{bed}	bed surface (m^2)
44	A_{BD}	area of secondary reflector (m^2)
45	A_{LFR}	area of primary LFR (m^2)
46	$A_{p,sL}$	effective heat transfer area at the top bed (m^2)
47	b	semiminor axis (m)
48	c	semidistance between hyperbola foci (m)
49	Cp	specific heat capacity (J/kgK)
50	d_p	particle diameter (μm)
51	e	hyperbola eccentricity (-)
52	f_{curv}	focal length of each mirror (m)
53	G_b	direct normal irradiation (W/m^2)
54	F_{ij}	view factor (-)
55	H_{focus}	hyperbola focus (m)
56	H_{rec}	receiver height (m)
57	H_{bed}	static bed height (m)
58	h	enthalpy (kJ/kg)
59	k_e	effective thermal conductivity (W/mK)
60	k_r	radiative conductivity (W/mK)
61	K	excess air velocity (-)
62	$L_{arc,hyp}$	hyperbola arc (m)
63	L_{line}	length of one LPSR line (m)
64	$\dot{m}_{sand}$	sand mass flow (kg/s)
65	N_{LFR}	number of primary linear Fresnel reflectors (-)
66	N_{lines}	number of LPSR lines (-)
67	N_{units}	number of units of a LPSR line (-)
68	P	performance parameter (kW/m^2)
69	$q_{BD}(x)$	flux intensity distribution on the receiver (W/m^2)

$Q_{air,out}$ heat gained by the fluidizing air through the bed (W)

Q''_{BD} heat flux on the receiver (W/m^2)

Q'''_{bbs} heat gained by bubbles (W/m^3)

$Q'''_{conv,loss}$ heat losses to the surroundings due to convection (W/m^3)

Q'''_{gs} heat gained by emulsion gas (W/m^3)

Q''_{in} heat flux on the bed surface (W/m^2)

Q_{loss} heat losses to the surroundings due to convection and radiation (W)

Q'''_{net} net heat gained on the bed surface (W/m^3)

$Q'''_{r,out}$ radiative heat loss from the bed surface (W/m^3)

Q'''_{sand} heat gained by the mass flow of particles (W/m^3)

$R_{\dot{m}}$ particles to air mass flow ratio (-)

T temperature (ºC)

U air velocity (m/s)

U_0 air velocity (m/s)

U_{mf} minimum fluidization velocity (m/s)

w_{hyp} width of the hyperbola (m)

w_{LFR} width of primary linear Fresnel reflectors (m)

w_{rec} width of the LPSR (m)

x horizontal coordinate (m)

$Y_{hyp}(x)$ secondary mirror function

z vertical direction (m)

Greek symbols

α_{bed} effective bed absorptivity (-)

ΔP pressure drop (bar)

ε emissivity (-)

ε_e emulsion void fraction (-)

ε_{eff} effective bed surface emissivity (-)

η efficiency (%)

ρ density (kg/m^3)

ϕ particle sphericity (-)

σ	Stefan-Boltzmann constant (W/m^2K^4)
τ_{eff}	effective transmissivity (-)

Subscripts

amb	ambient
b	bubble
BD	beam-down
comp	compressor
conv	convection
curv	curved mirror
d	distributor
e	emulsion
g	gas
glass	glass cover
hyp	hyperbola
p	particle
rad	radiation
rec	receiver
s	solids
SF	solar field
th	thermal
wall	receiver wall

1. Introduction

The potential of applying solar energy for industrial purposes is still largely untapped. Using solar energy through Concentrating Solar Technologies (CST) to provide the heat necessary to industrial processes requires innovative solutions (Mekhilef et al., 2011). Besides, Concentrating Solar Power (CSP) plants are a promising technology that may supply the increasing electricity demand in a clean and renewable way (IRENA, 2017) . However, the reduction in price of other energy sources, such as photovoltaic or wind technology, makes necessary to improve its performance. One pathway to improve the versatility of CST is the increase of the absorption temperature of the heat transfer fluid (HTF) (Mehos et al., 2017). Solar thermal energy for industrial processes, thermochemical processes, lime production and applications for materials science and metallurgy may be explored through CST at temperatures of 200-1200 ºC (Mekhilef et al., 2011) (Yadav and Banerjee, 2016) (González et al., 2018). Similarly, CSP technology shows temperatures of 565 ºC in solar tower plants employing molten salts (60% KNO_3 and 40% $NaNO_3$), which is the most efficient commercial CSP technology.

One option to increase the hot HTF temperature of CSP plants is to substitute molten salts by particles as HTF (Ho, 2016) (Calderón et al., 2018). The high thermal stability of particles, such as silicon carbide or silica sand, makes theoretically possible to reach temperatures near 1000 ºC without HTF degradation, which enhances its use for thermal energy storage (TES). Furthermore, this high temperature would open the integration of CSP with high efficiency power cycles, such as supercritical-CO_2 (sCO_2) (Fernández-Torrijos et al., 2018) (Stein and Buck, 2017), ultra-supercritical steam-cycles (Stein and Buck, 2017), air Brayton cycles (Korzynietz et al., 2016) or thermochemical processes (Yadav and Banerjee, 2016). With this aim, the national laboratories of SANDIA (US), DLR (Germany) and CNRS-Promes (France) have presented particle receiver designs that stand out for their promising results. Current receiver designs can be grouped into free falling particle receiver, rotary receiver and confined fluidized bed receiver.

All these designs have in common the solar field configuration. These particle receivers are placed on top of a central tower, where 2-axis heliostats focus the concentrated energy. For free-falling particle receivers, particles are directly irradiated by concentrated sunlight while falling forming a curtain (Ho and Iverson, 2014). This approach showed bulk temperatures near 800 ºC for mass flow rates of 1 – 3 kg/s (Ho et al., 2017) (C. Ho et al., 2018), although the reduction of particle loss through the aperture is still under development. The residence time of particles can be increased employing obstructed flow receivers with chevron-shaped mesh structures, reaching 660 ºC for ~ 2 kg/s of particles mass flow. However, issues were found on the deterioration of the mesh structures (C. K. Ho et al., 2018). Other tower-top design, a rotary particle receiver, employs an inclined drum placed on top of a central tower that rotates while particles fall attached to the drum walls (Wu et al., 2014). Temperatures of 965 ºC for a mass flow range of 0.15 – 0.18 kg/s have been achieved (Ebert et al., 2018). Particle loss trough the receiver aperture and the scaling-up are the main challenges of this design (Ho, 2016). The last design consists of an upward fluidized bed confined in vertical tubes that receives the concentrated energy on the exterior of the tube wall (Benoit et al., 2015). The mixture of fluidizing air and particles reaches temperatures of 750 ºC while flowing vertically.

All the aforementioned particle receivers are able to reach promising high temperatures. However, other researchers have placed the receiver at the ground level to ease its maintenance and operation works (Yadav and Banerjee, 2016). To that end, a secondary reflector, or beam-down, is placed on top of a tower to redirect the impinging light towards the ground. Segal and Epstein showed that a beam-down tower could reach concentrations above 1800 kW/m^2 on the ground receiver (Segal and Epstein, 2001). The main drawback of the beam-down system is the large magnification of the image due to the hyperbolic shape of the secondary reflector. As stated by Vant-Hull (Vant-Hull, 2014), the costs associated to the construction of the secondary reflector may be high, and also, compound parabolic concentrators (CPCs) are usually needed to recover the lost magnification (Kodama et al., 2016). Therefore, a cost-benefit analysis of each process must be carried out to justify the modification of the tower-top receivers to a beam-down approach.

Many examples in the literature show that current beam-down optics is an attractive technological solution to drive power cycles or for thermochemical processes. Current beam-down optics can be coupled to a direct absorption molten salt receiver (Calvet et al., 2016). Other designs use particles as HTF and storage media due to its high thermal stability. Although there are many designs (Ermanoski et al., 2013) (Iniesta et al., 2015) (Xiao et al., 2014), fluidized bed technology stands out as solar receivers due to its high heat and mass transfer coefficients (Almendros-ibáñez et al., 2018). In this sense, a beam-

down tower pilot plant using a 2 MW_{th} fluidized bed power receiver with 6 hours of thermal storage can be found in (Chirone et al., 2017) (Magaldi, n.d.). Temperatures near 1200 ºC have been achieved in a fluidized bed receiver coupled with a beam-down tower solar field (Kodama et al., 2014) (Kodama et al., 2017). Furthermore, fluidized bed reactors have been combined with CSP for coal gasification (Gokon et al., 2014), water-splitting (Gokon et al., 2008), and thermochemical energy storage or calcium looping cycles (Chacartegui et al., 2016) (Ortiz et al., 2017) (Tregambi et al., 2018).

From the current literature state, the first question that arises is if, considering the limitations of tower-top particle receivers and the constraints of building a high central tower for current beam-down optics, there is a solar field layout able to redirect the concentrated energy to the ground level. The second question is if the ground receiver is able to reach high particle temperatures meeting the industry requirements. To solve the first question, this work explores the advantages of linear Fresnel (LFR) technology, such as its simple and cheap sun tracking system, with a new Beam-Down Linear Fresnel Reflector (BDLFR) optic system (Gómez-Hernández et al., 2017). From the economic point of view, the new configuration of the solar field is justified by the low costs of linear Fresnel heliostats (Marugán-Cruz et al., 2018). The second question is solved designing a new linear particle solar receiver (LPSR) that consists of multiple connected fluidized bed receivers placed below the BDLFR. Concentrated solar energy from the BDLFR solar field irradiates linearly the fluidized beds through glass covers. The fluid-like behavior of the air-particles mixture allows the horizontal movement of particles through the vessel openings of the units that compose the LPSR (Kunii and Levenspiel, 1991). This design was introduced by the authors in (Gómez-Hernández et al., 2017) (Santana et al., 2017) (Sánchez-González and Gómez-Hernández, 2020) and analyzed here.

In this work, the feasibility of the new linear particle solar receiver is studied analyzing the temperatures of both the air and the particles mass flows as a function of the solar field and particle receiver geometries. To simplify the analysis, the BDLFR solar field is based on Fresdemo Fresnel design (Bernhard et al., 2008), which is modified changing the absorber tube by a linear beam-down secondary reflector. The width and eccentricity of the secondary beam-down concentrator, and the receiver dimensions are studied for both flat and curved primary mirrors. Once the heat flux on the receiver is known, the performance of a LPSR is evaluated as a function of the receiver dimensions for different industrial applications. Target bed temperatures of 200 ºC, 400 ºC, 600 ºC and 800 ºC have been studied reproducing the CST integration with industry applications, such as medium and high temperature process heat, Rankine CSP and sCO_2 cycles, respectively.

2. BDLFR and LPSR system

The CST layout proposed is comprised by three subsystems: an air compressor, the BDLFR solar field and the linear particle solar receiver, Fig. 1. The following sections describe first the BDLFR solar field layout pointing out the two cases considered: flat and curved primary heliostats. Then, the linear particle solar receiver is described.

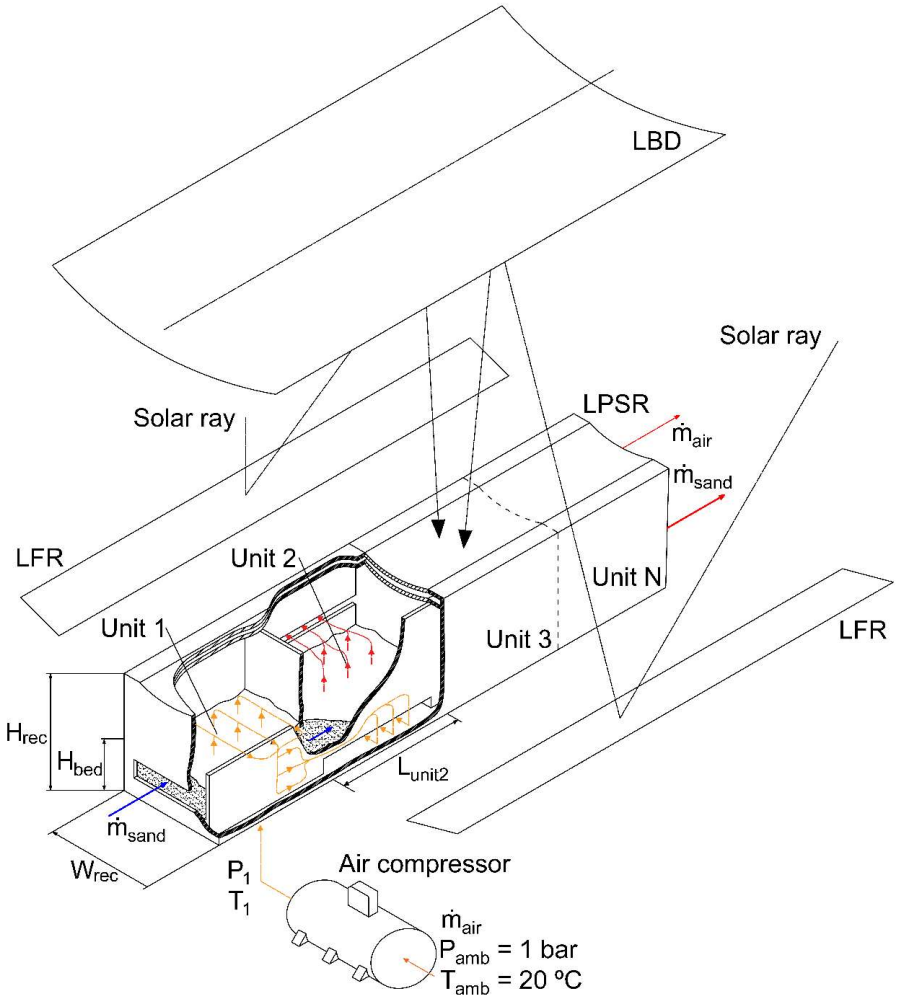

Figure 1. Conceptual sketch of the Linear Particle Solar Receiver coupled to the proposed LBDFR solar field.

2.1 LBDFR solar field

The solar field is formed by a primary field of Fresnel heliostats and a secondary concentrator, the linear beam-down reflector. As shown in Fig. 2, the layout of the primary mirrors is based on Fresdemo design employing N_{LFR} = 24 mirrors of w_{LFR} = 0.6 m width that are placed at 2 m height above the ground (Bernhard et al., 2008). Compared to Fresdemo design, Fig. 2 introduces the following changes:

- The substitution of the absorber tube placed at H_{focus} = 8 m by the first focus of the linear beam-down concentrator, which section follows a hyperbola, Eq. (1). This secondary reflector is a hyperbolic cylinder as this geometry has the property that any ray pointed to the focus is redirected to the second focus, where the ground receiver is placed.

$$Y_{hyp}(x) = \frac{a}{b}\sqrt{x^2 + b^2} + \frac{H_{focus}}{2} \qquad \text{Eq. (1)}$$

The beam-down reflector is defined by its semimajor axis *a* and its semiminor axis *b*, which are related by the definition of the first focus height and the eccentricity *e*, Eqs. 2-3.

$$H_{focus} = 2c = 2 \cdot \sqrt{a^2 + b^2} \quad \text{Eq. (2)}$$

$$e = \frac{c + a}{H_{focus}} = 0.5 + \frac{a}{2c} \quad \text{Eq. (3)}$$

- The central primary reflector of Fresdemo layout has been removed, placing the linear particle solar receiver. The receiver width (w_{rec}) will be analyzed as a function of the beam-down dimensions.

- LFR primary heliostats are composed by flat or slightly curved primary mirrors. Each curved primary mirror ($Y_{mirror,curv}(x)$) is defined as a function of the focal length of each mirror (f_{curv}), Eqs. (4-5). The maximum deflection of these mirrors is 2 mm, making easy its bent (Abbas et al., 2012) (Abbas and Martínez-Val, 2017).

$$f_{curv} = \sqrt{x_i^2 + H_{focus}^2} \quad \text{Eq. (4)}$$

$$Y_{mirror,curv}(x) = \frac{1}{2} \cdot \frac{1}{2f_{curv}} \cdot x_i^2 \quad \text{Eq. (5)}$$

where x_i is the position of each mirror center (Fig. 2).

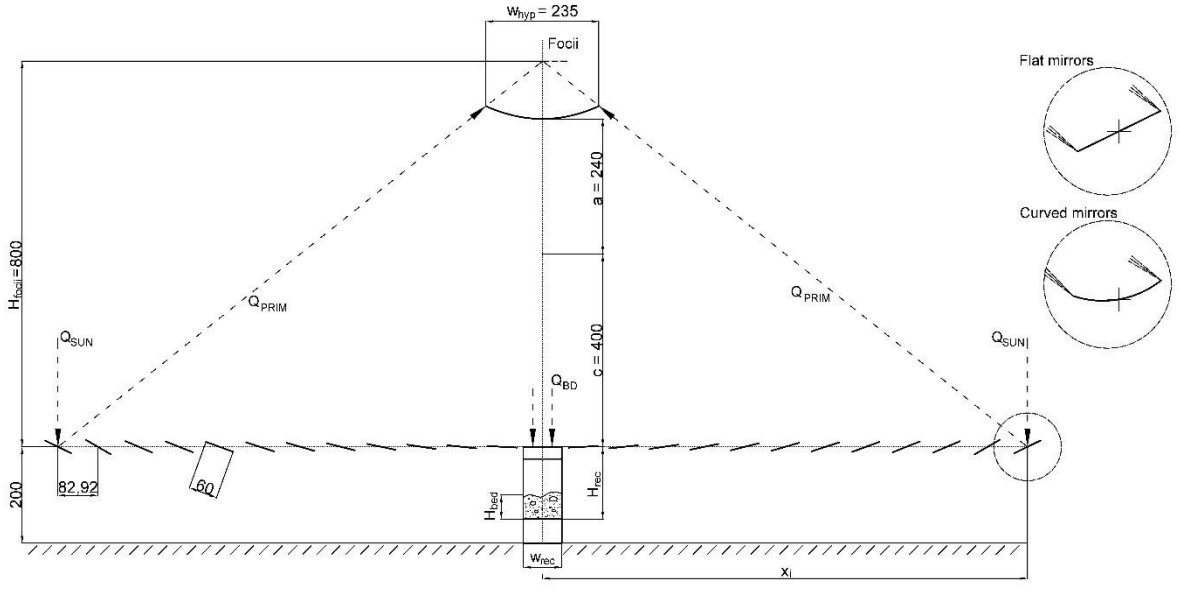

Figure 2. Linear beam-down solar field with 24 primary mirrors of 60 cm width, which can be flat or slightly curved, oriented in N-S direction, eccentricity *e* = 0.85. All dimensions in cm.

2.2 Linear Particle Solar Receiver

A LPSR consists of multiple fluidized bed units (N_{units}) connected linearly. Each unit is formed by a distributor plate, an inner vessel that contains the bed of particles, an exit for

the fluidizing air, an exterior vessel that redirects the airflow to the next unit and 2 glass covers (Santana et al., 2017), Fig. 3. Vacuum conditions are assumed between the covers in order to reduce the heat losses.

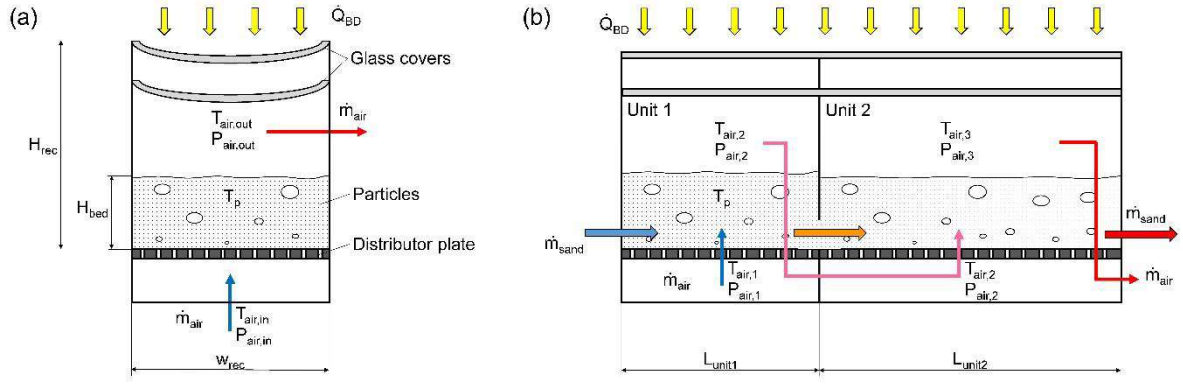

Figure 3. Sketch of a receiver unit with arrows pointing the solar radiation, gas and particle mass flows for (a) front section view and (b) longitudinal section view.

Table 1 summarizes the characteristics of the proposed layout. The effect of the refraction index of both glass covers is considered in the effective glass transmissivity, $\tau_{eff,glass}$. Therefore, the heat flux in the bed surface is simplified to $Q''_{in} = \tau_{eff,glass} \cdot Q''_{BD}$.

Table 1. Summary of solar field and particle receiver characteristics.

BDLFR solar field		
Number of primary LFR, N_{LFR} (-)		24
Heliostat width, w_{LFR} (m)		0.6
Hyperbola focus, H_{focus} (m)		8
LPSR		
Compressor inlet air temperature (ºC)		20
Particles inlet temperature (ºC)		20
Air compressor efficiency, η_c (%)		80
Receiver height, H_{rec} (m)		1.5
Bed aspect ratio, H_{bed}/w_{rec} (-)		0.25
Excess air velocity, $K = U_0/U_{mf}$ (-)		2 - 4
Outlet air pressure, $P_{air,end}$ (bar)		1.1
Glass covers	transmissivity, $\tau_{eff,glass}$ (-)	0.83
	emissivity, ε_{glass} (-)	0.86
Vessel wall emissivity, ε_{wall} (-)		0.86

Several units will be connected forming a process line. The fluidizing air flows consecutively from the first to the last unit on each line. The compressed air enters from

the bottom of the unit, flowing upwards through the distributor and fluidizing the particles, Fig. 3-a. This air enters to the LPSR at T_1 and P_1, which values depend on the line length. A mass flow of particles enters to the first unit of the LPSR at T_{amb} = 20 ºC.

From the receiver top, the concentrated energy (Q''_{BD}) is transmitted through the glass covers, which present an effective transmissivity of $\tau_{eff,glass} = 0.83$. Particles absorb the energy while heating up the fluidizing air. Air flows vertically through the bed, ensuring the fluid-like behaviour of the particles (Kunii and Levenspiel, 1991). As air pressure of vessel 1 is greater than air pressure of vessel 2, particles are moved horizontally with low void fraction through the vessel openings that connect all units (Chong et al., 1986), Fig. 3-b. A negligible air leakage through the vessel openings is expected, less than 2% of gas mixing according to (Chong et al., 1986). Examples of solids movement between fluidized beds can be found in (Bhattacharya et al. 1999) (Kong et al., 2018) (Kunii and Levenspiel, 1991) (Kuramoto et al., 1985, 1986) (Mujumdar, 2014). The exit hot air flows to the following unit through the exterior vessel, absorbing energy from the particles until the thermal equilibrium is reached.

Once the particles are at the end of the line, the sand mass flow may return to the initial unit using a conveyor belt system, which can be optimized to reduce its parasitic consumption. Further design details can be found in (Gómez-Hernández et al., 2017) (Santana et al., 2017) and in the video supplementary material.

Regarding the geometry of the receiver, its width (w_{rec}) depends on the beam-down eccentricity. Each unit length (L_{unit}) depends on the air mass flow and the fluidization regime. The receiver height (H_{rec}) is set to 1.5 m as, on the one hand, it reduces the view factor between the bed surface and the glass covers, and, on the other hand, there is enough space below the primary heliostats for the plenum chamber. The bed aspect ratio is fixed to $H_{bed}/w_{rec} = 0.25$ in order to ensure good fluidization conditions at the minimum pressure drop (Kunii and Levenspiel, 1991). Furthermore, a bubbling fluidized regime is achieved keeping the excess air velocity between $U_0 = 2 \cdot U_{mf}$ and $U_0 = 4 \cdot U_{mf}$. Silica sand particles are used due to its high thermal stability for a wide range of temperatures, its easy integration as thermal energy storage media and its low cost (Diago et al. 2018). Table 2 summarizes the properties of the silica sand particles employed, showing their reference temperatures. The bulk density of the fluidized bed is calculated according to (Kunii and Levenspiel, 1991).

Table 2. Silica sand properties (Kunii and Levenspiel, 1991) (Mazza et al., 1991).

Diameter, d_p (μm)	Sphericity, ϕ (-)	Particle density, ρ (kg/m^3)	Specific heat capacity at T = 293K, *Cp* (J/kgK)	Particle emissivity at T = 293 – 1000 K, ε_p (-)	Bed absorptivity at T = 293 – 1000 K, α_{bed} (-)
250	0.71	2,650	1,250	0.36 - 0.77	0.5 – 0.85

3. Methodology

This section describes the procedure followed to study the performance of the LPSR. The methodology is summarized in Fig. 4. First, the BDLFR solar field is analyzed, obtaining

the dimensions of the hyperbola and the receiver width using SolTrace (Wendelin et al., 2013). This gives the input to the LPSR model, i.e. the concentrated solar energy on each fluidized bed and the receiver width. Then, an iterative procedure is employed to solve the thermal network and the energy balance equations at steady state for each unit. Note that the thermal network combines convection and radiation heat transfer mechanisms, as shown in (Duffie et al., 2003) (Vasquez et al., 2011). The line length (L_{line}) and the sand mass flow ($\dot{m}_{sand}$) are the variables used to analyze the LPSR performance as they will modify the temperature profiles on the receiver. Finally, different target temperatures are analyzed to study the LPSR integration with several industrial purposes.

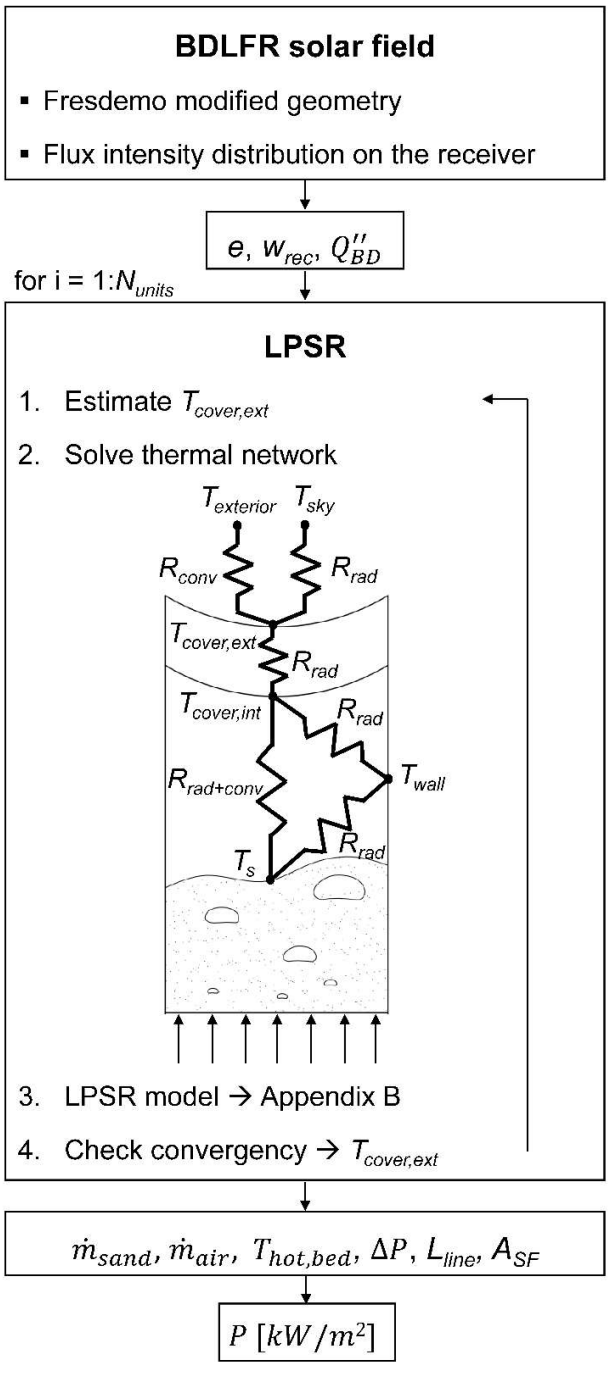

Fig. 4. Conceptual scheme of the model.

3.1 Solar field analysis

A ray tracing software, SolTrace (Wendelin, 2003), is used to analyze the optical performance of the BDLFR optics. As the solar field layout is based on Fresdemo design, the position of the primary mirrors and the height of the hyperbola focus are considered fixed (Bernhard et al., 2008). The eccentricity of the beam-down reflector (Eq. 3) is the main variable used to define the dimensions of the hyperbola and the receiver width for both flat and curved primary mirrors. To that end, the energy distribution on the receiver is analyzed as a function of both the eccentricity and the receiver width. The solar field efficiency is calculated according to:

$$\eta_{SF} = \frac{\int_{-w_{rec}/2}^{w_{rec}/2} q_{BD}(x)\, dx}{G_b \cdot N_{LFR} \cdot w_{LFR}} = \frac{Q''_{BD} \cdot w_{rec}}{G_b \cdot N_{LFR} \cdot w_{LFR}} \qquad \text{Eq. (6)}$$

where $q_{BD}(x)$ is the flux intensity distribution on the receiver.

Regarding the eccentricity, it modifies the width of the hyperbola (w_{hyp}), which is calculated as the intersection between the reflected ray of the last row and the hyperbola function (Eq. 5). As shown in Fig. 5, an eccentricity of *e* = 0.5 means a flat secondary reflector with high width ($w_{hyp} = 10.1\ m$) that should be installed at a height of $a + c = 4\ m$ above the outer receiver glass cover, i.e. at 6 m above the ground level. As the position of the primary mirrors are fixed, the high hyperbola width means a high shadow. On the contrary, *e* = 0.9 shows a sharp and narrow hyperbola ($w_{hyp} = 1.6\ m$) that should be installed at 9.2 m above the ground.

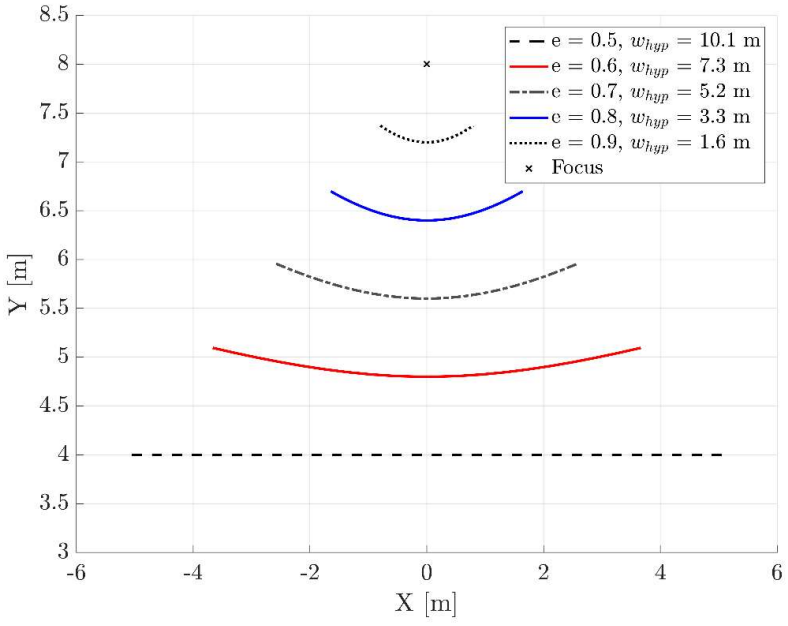

Figure 5. Beam-down secondary reflector dimensions as a function of its eccentricity.

The simulation runs are carried out the 21st of March assuming G_b = 1000 W/m^2 at noon, Fig. 6. The selected location is Puerto Errado II (Spain) (38.278 latitude and -1.6 longitude) ("Puerto Errado 2 Thermosolar Power Plant," n.d.). Sun shape is modeled as a distribution close to pill-box with a cone semi-angle of 4.65 mrad and using 10^7 ray intersections (Buie et al., 2003). Primary and secondary reflectors are characterized by a

reflectivity of 0.94, Gaussian error distributions of 2 mrad for slope error and 1.5 mrad for specularity error (Kincaid et al., 2019) (Zhu and Lewandowski, 2012).

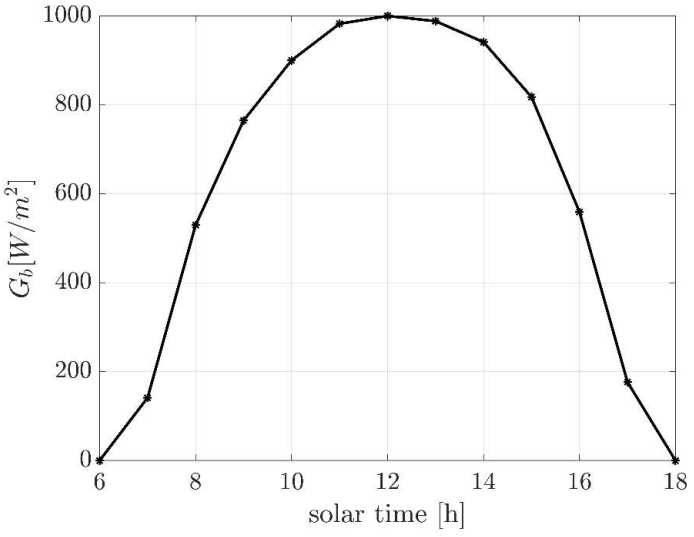

Figure 6. Direct solar irradiation (G_b).

3.2 Fluidized bed receiver model

Each fluidized bed is solved following the two-phase model described in (Briongos et al., 2018) with the following assumptions:

- Steady-state conditions.
- Vacuum conditions between the glass covers.
- Fluidization operation at the bubbling regime between K = 2 - 4.
- Emulsion phase formed by interstitial gas and particles (Kunii and Levenspiel, 1991).
- Bubble phase formed by bubbles and the gas through-flow (Kunii and Levenspiel, 1991).
- Bubble size calculated according to (Mori and Wen, 1975).
- Homogeneous distribution of energy on the bed surface (Briongos et al., 2018).
- Bed surface considered as an opaque diffuse layer formed by gray particles (Mazza et al., 1991).
- Bed voidage changes with temperature and particle properties (Formisani et al., 1998).
- Well-stirred conditions for the particles leaving each bed (Kunii and Levenspiel, 1991).
- Sand mass flow moves horizontally due to the fluidized state (Kunii and Levenspiel, 1991) (Fang et al., 2003).
- No leakage or gas-by pass of the fluidizing air through the horizontal openings between units (Chong et al., 1986).

- Heat losses to the surroundings due to convection are the 5% of the incoming irradiation per unit of bed surface.

According to this model (Briongos et al., 2018), the first law of thermodynamics is applied to both the emulsion phase and the bubble phase. The equations are described in Appendix B.

A thermal network is considered to solve the re-radiant heat transfer problem of the system formed by the two glass covers, the inner vessel walls and the gray-diffuse bed surface, Fig. 4. An iterative process is employed to solve this thermal network (Duffie et al., 2003):

1- Estimate the exterior glass cover temperature.

2- Calculate the radiation and convection heat transfer coefficients between the ambient and the exterior glass cover, between glass covers, and between the inner glass cover, the inner vessel walls and the bed surface.

3- Solve the energy balance equations (Appendix B).

4- Check the exterior glass cover temperature and iterate until convergence, i.e. 1% of relative error.

The thermal efficiency of a LPSR line is calculated as:

$$\eta_{th,rec} = 1 - \frac{\sum_{i=1}^{N_{units}} Q_{loss,i}}{Q''_{BD} w_{rec} L_{line}} \quad \text{Eq. (7)}$$

where $Q_{loss,i}$ describes the heat losses by radiation through the exterior glass cover and the heat losses by convection with the surroundings ($Q'''_{conv,loss}$). L_{line} is the sum of all unit lengths that compose a line, Eq. 8.

$$L_{line} = \sum_{i=1}^{N_{units}} L_{unit,i} \quad \text{Eq. (8)}$$

As the mass flow of air is kept constant throughout the line, the decrease of air pressure and the increase of air temperature reduces both the air density and the minimum fluidization velocity, making necessary to increase the length of the units to maintain a bubbling fluidization regime. This is achieved fixing a range for the excess gas velocity of $K = 2 - 4$. Thus, when $K = 4$ is reached, the unit length is increased according to Eq. 9 to reduce the airflow velocity. A unit length of $L_{unit,1} = 0.5\ m$ is set for the first unit to initialize the LPSR calculations.

$$L_{unit,i} = L_{unit,i-1} + L_{unit,1} \quad \text{Eq. (9)}$$

3.3 Performance analysis

The behavior of both the BDLFR and the LPSR is studied considering the geometry of the receiver, its width and length, and the mass flow of particles as variables. The receiver width is coupled with the incoming flux of energy from the secondary reflector, which value changes with the hyperbola eccentricity. Such an influence is studied using SolTrace. Furthermore, the performance of the BDLFR and the LPSR geometry is analyzed considering target bed temperatures of 200 ºC, 400 ºC, 600 ºC and 800 ºC.

The fluidized state of the particles allows the continuous mass flow of sand through the units (Kunii and Levenspiel, 1991). At steady-state conditions, the sand mass flow that enters into a bed is equal to the sand mass flow that leaves the bed. Furthermore, as well-stirred conditions are considered, the outlet temperature of the sand mass flow is the same temperature of the bulk bed. This hypothesis can be assumed only for low sand mass flows (Davidson et al., 1963, 1985). Otherwise, the residence time distribution of particles should be estimated (Geng et al., 2017) (Hua et al. 2019), as the bulk temperature would be different to the outlet sand mass flow temperature. Following a conservative approach to obey the well-stirred assumption, the sand mass flow per line is fixed depending on the receiver width. Table 3 shows the values selected. Cases A, B, and C can be compared as the ratio between the sand mass in the bed and the sand mass flow, $m_{bed}/\dot{m}_{sand}$, is kept constant.

Table 3. Receiver widths and sand mass flows studied.

Receiver width, w_{rec} [m]	Sand mass in the bed, m_{bed} [kg]	Sand mass flow, $\dot{m}_{sand}$ [kg/s]		
		Case A	Case B	Case C
0.5	35	0.175	0.35	1.75
1	140	0.7	1.4	7

Regarding the compressor power, the inlet pressure (P_1) to the LPSR is calculated using Eq. 10, where the distributor pressure drop (ΔP_d) and the bed pressure drop (ΔP_{bed}) are estimated from (Kunii and Levenspiel, 1991). The air outlet pressure is set to $P_{air,end} = 1.1\ bar$, while air enters to the compressor at $P_{amb} = 1\ bar$ and $T_{amb} = 20$ ºC.

$$P_1 = P_{air,end} + N_{units} \cdot (\Delta P_d + \Delta P_{bed}) \quad \text{Eq. (10)}$$

The solar field aperture area is calculated considering both the primary and the secondary reflectors, Eq. 11.

$$A_{SF} = A_{LFR} + A_{BD} = \left(w_{LFR} \cdot N_{LFR} + L_{arc,hyp}\right) \cdot L_{line} \quad \text{Eq. (11)}$$

where $L_{arc,hyp}$ varies with the eccentricity. The heat gained by air and sand is calculated considering the outlet temperature of the compressor (T_1) as a reference, Eqs. 12-14. This air temperature depends on the compressor pressure ratio, which increases with the length of the line. Similarly, the compressor work is calculated using Eq. 14.

$$Q_{air} = \dot{m}_{air} \cdot Cp_{air} \cdot (T_{air,N} - T_1) \quad \text{Eq. (12)}$$

$$Q_{sand} = \dot{m}_{sand} \cdot Cp_{sand} \cdot (T_{bed,N} - T_1) \quad \text{Eq. (13)}$$

$$W_{comp} = \dot{m}_{air} \cdot (h_1 - h_{amb}) \quad \text{Eq. (14)}$$

The performance of the solar field and the particle receiver is studied defining *P* parameter, Eq. 15. A conveyor belt system may be used to return the particles to the initial unit. However, its consumption is negligible compared to the compressor work, and due to that, it has been neglected in Eq. 15. This efficiency parameter relates the useful heat

power obtained from the LPSR with the total aperture area of the BDLFR (Eq. 11). As the solar field usually represents the most expensive part of a CST plant, this parameter may give a first insight of the system costs.

$$P = \frac{Q_{air} + Q_{sand} - W_{comp}}{A_{SF}} \qquad \text{Eq. (15)}$$

4. Results

First, the BDLFR solar field is analyzed obtaining the incoming concentrated radiation on the outlet glass cover (Q''_{BD}) as a function of the eccentricity of the hyperbola and the receiver width. Then, the new LPSR design is analyzed studying the influence of the receiver width and the sand mass flow on the particle receiver performance. The receiver width, hyperbola width, sand mass flow and aperture area are considered for different bed temperatures.

4.1 Solar field and receiver dimensions

The flux intensity distributions for flat and curved primary mirrors are shown in Fig. 7 as a function of the receiver width and the hyperbola eccentricity. Both cases show that flat secondary reflectors (*e* = 0.5) present the highest energy concentrations although the shadow of the hyperbola on the primary reflectors is maximum (Fig. 5). Furthermore, the higher the eccentricity, i.e. the sharper the hyperbola, the lower the peak flux intensity on the receiver. This magnification lost is caused as only the rays that reflect in the center of the primary mirrors are aiming directly to the hyperbola focus. However, the rays reflected in the primary mirror edges may fall far from the particle receiver (Vant-Hull, 2014).

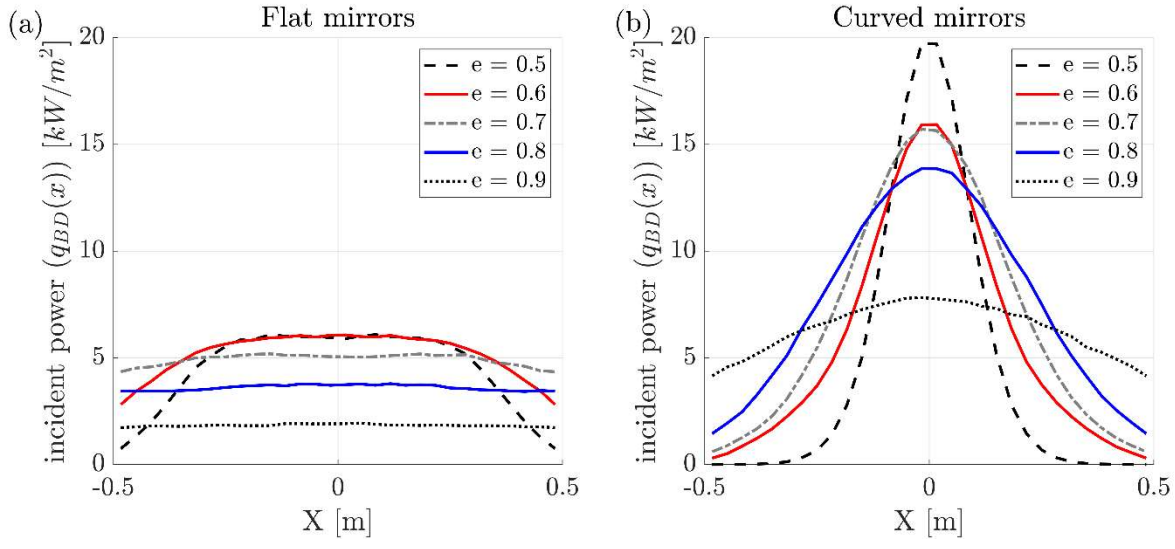

Figure 7. Flux intensity distributions for (a) flat primary mirrors and (b) curved primary mirrors.

Flat primary mirrors (Fig. 7-a) present flat energy distributions on the ground receiver with maximum values of 6.2 kW/m^2 for eccentricities of *e* = 0.5 - 0.6. The tails of the energy distribution disappear as the eccentricity increases due to the increase of spillage. Higher flux intensities are shown for curved primary mirrors (Fig. 7-b), with a peak for a flat hyperbola (*e* = 0.5) in a narrow receiver. However, when the eccentricity increases, the shadow of the hyperbola decreases (Fig. 5), and thus, more energy can reach the LPSR depending on its width.

Figure 8 shows the solar field efficiency, calculated using Eq. (6), for the eccentricities considered and for different receiver widths. The low flux intensity distributions shown by flat primary mirrors lead to low solar field efficiencies, Fig. 8-a. In contrast, curved mirrors (Fig. 8-b) show higher efficiencies than flat mirrors. On the one hand, when the eccentricity increases, less primary reflectors are under shadow although the reflected image on the ground is magnified. On the other hand, the increase of the receiver width improves the solar field efficiency up to almost constant values. Fig. 8-b shows that a high efficiency of $\eta_{SF} = 53.33\%$ is reached for a receiver width of w_{rec} = 1 m and an eccentricity of e = 0.8.

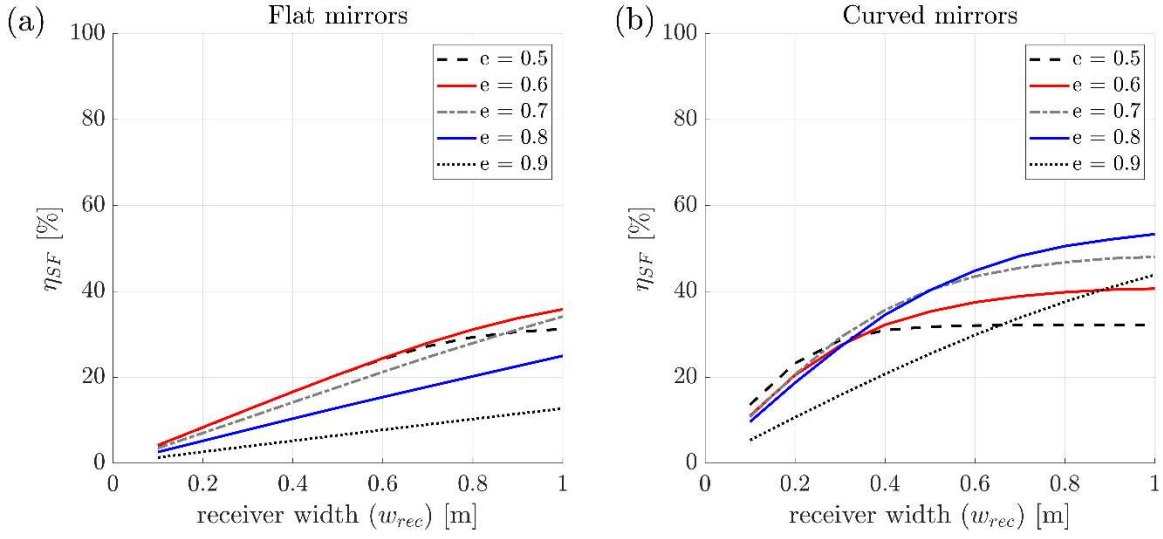

Figure 8. Solar field efficiency for different receiver widths: (a) flat primary mirrors and (b) curved primary mirrors.

Eq. 6 can be also used to calculate the average heat flux (Q''_{BD}) on the LPSR. Figure 9 shows this result for flat and curved primary mirrors. Fig. 9-a shows that flat primary LFR can be disregarded due to the low average heat flux achieved. Focusing on Fig. 9-b for curved mirrors, the average heat flux greatly depends on the receiver width and hyperbola eccentricity. For instance, a wide hyperbola with e = 0.5 coupled with a narrow LPSR of $w_{rec} = 0.2\ m$ presents a high average heat flux of $Q''_{BD} = 16.75\ kW/m^2$. However, the efficiency of this case is only $\eta_{SF} = 23.3\%$ (Fig. 8-b) as the hyperbola width is $w_{hyp} = 10.1\ m$ (Fig. 5). This result is explained by the low image magnification on the receiver. Higher receiver widths show the maximum concentration at an eccentricity of e = 0.8 (Fig. 9-b), which also presents the maximum solar field efficiencies (Fig. 8-b).

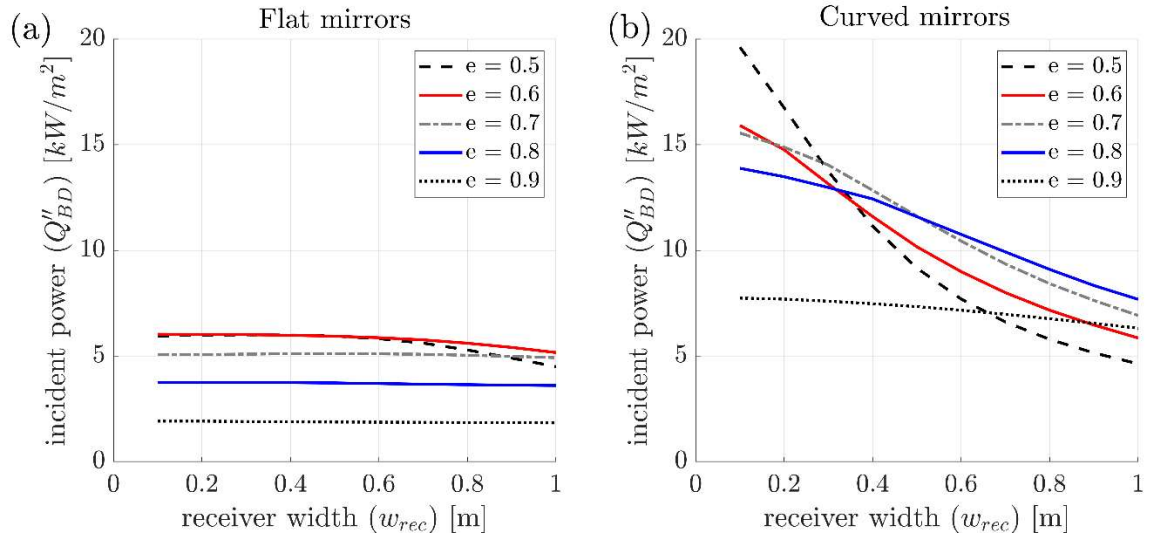

Figure 9. Average heat flux on the particle receiver for: (a) flat primary mirrors and (b) curved primary mirrors.

Focusing on the solar field design employing curved primary mirrors, solar field efficiency and incident power results are shown in Fig. 10 as a function of the solar time. Although the BDLFR optic system is a modification of Fresdemo layout, and therefore its design is not optimized, the solar field performance shows a fairly constant behavior for all sunlight hours, Fig. 10-a. The incident power on the particle receiver as a function of the solar time is plotted in Fig. 10-b. Note the influence of the receiver width on the incident power, as commented before.

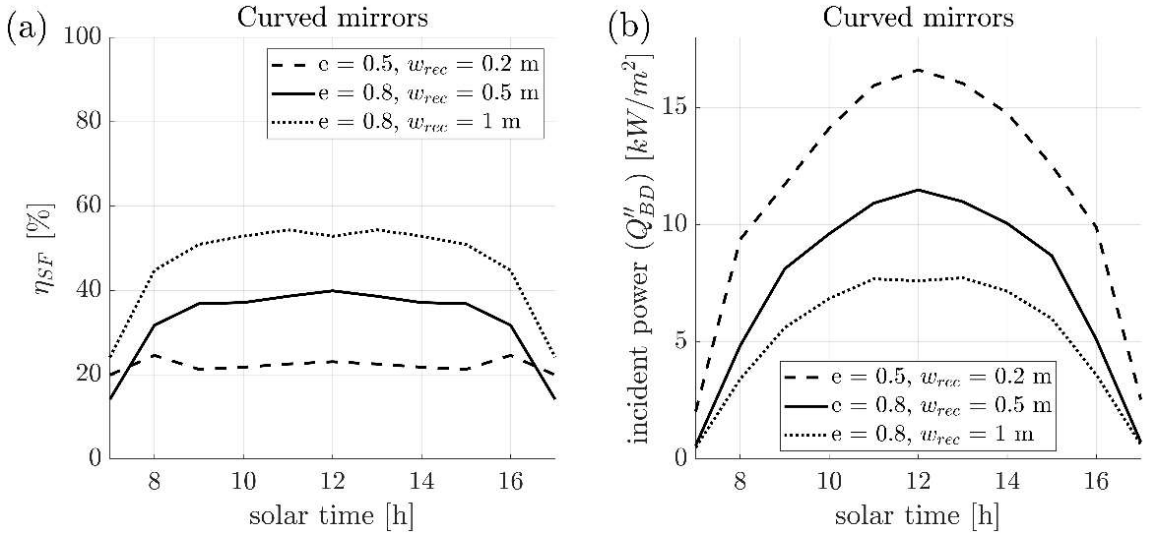

Figure 10. BDLFR performance as a function of the solar time for primary curved mirrors: (a) solar field efficiency and (b) incident power.

4.2. Linear particle solar receiver performance

Considering the average heat fluxes shown in Fig. 9-b and Fig. 10-b for curved primary mirrors, two opposite effects may determine the behavior of the LPSR. On the one hand, the narrower the receiver, the higher the concentration. This means high bed temperatures

but with low mass flows of air and particles. On the other hand, the wider the receiver, the higher thermal losses with the advantage of higher mass flow of air and particles. Therefore, the performance of the LPSR is studied considering these influences for different target temperatures.

To do so, two receiver widths and average flux intensities are considered at noon for a LPSR length of 350 m, which values are taken from Fig. 9-b:

(i) $w_{rec} = 0.5\ m$ and $Q''_{BD} = 11.49\ kW/m^2$.

(ii) $w_{rec} = 1\ m$ and $Q''_{BD} = 7.61\ kW/m^2$.

As the particle mass flow is calculated as a function of the receiver geometry, each width present different sand mass flows (Table 3). The following figures show the performance results of the cases considered. These figures show the sand to air mass flow ratios ($R_{\dot{m}}$), the bed temperature profiles and the thermal efficiencies of the LPSR (Eq. 7) and the performance parameter (*P*) (Eq. 15) as a function of the line length.

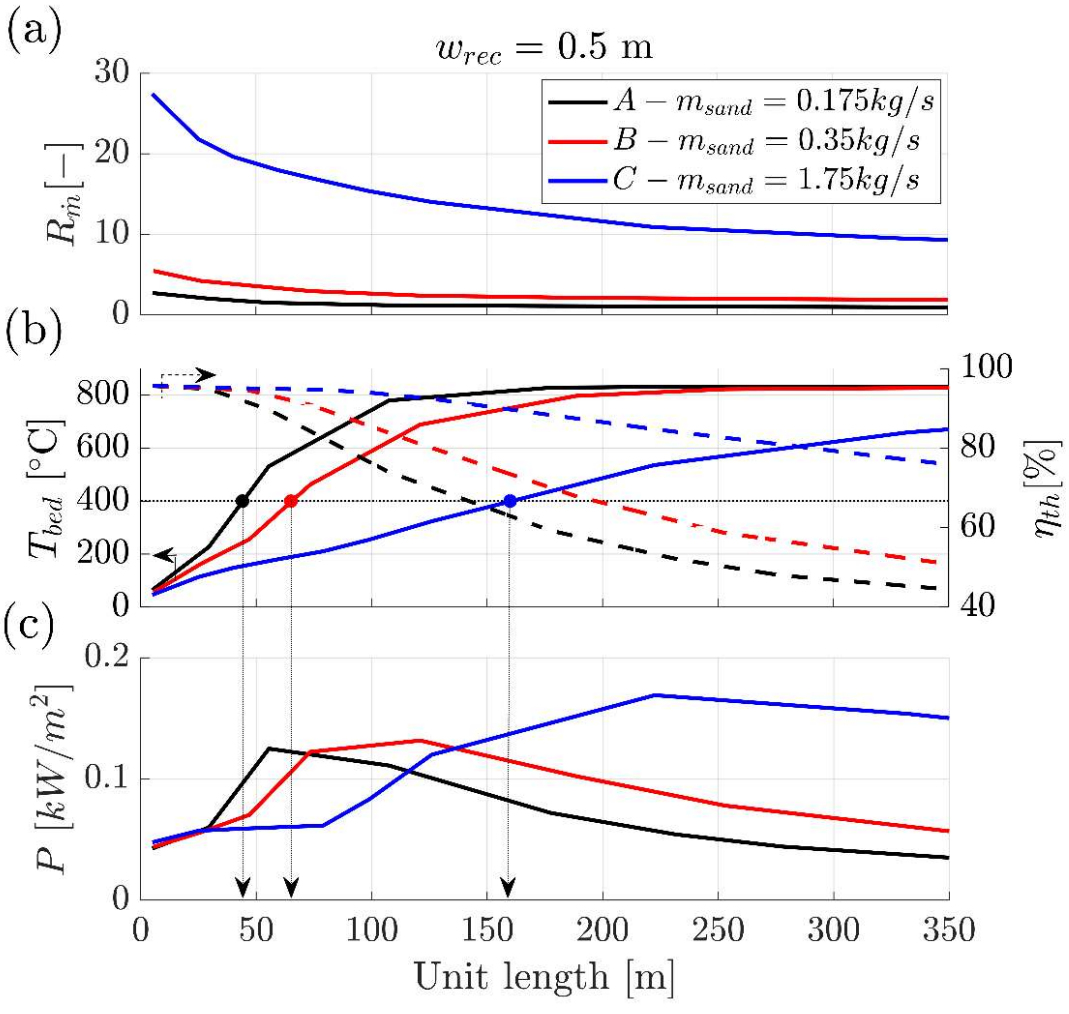

Figure 11. LPSR performance for $w_{rec} = 0.5\ m$: (a) sand to air mass flow ratio, (b) bed temperature and thermal efficiencies, (c) performance parameter. Arrows and dots illustrate the procedure to select the minimum aperture area with the maximum useful heat for a target temperature of 400 ºC.

Figure 11 shows the results for $w_{rec} = 0.5\ m$ and $Q''_{BD} = 11.49\ kW/m^2$, and an example to select the best configuration depending on the target temperature that will be explained later in Table 4. Fig. 11-a presents the values of the mass flow ratio. Note that these values change with the line length as the air density and the minimum fluidization velocity change with the inlet pressure to the LPSR (P_1 in Fig. 1). As the line length increases, the bed pressure drop and the gas distributor pressure drop increase, and thus, P_1 increases. Therefore, short lines may be preferred due to its low pressure drop and low BDLFR aperture area.

Fig. 11-b shows that temperatures above 800 ºC can be obtained for low sand mass flows (cases A and B). When the sand mass flow increases, the line length needed to reach the thermal equilibrium increases as well-stirred conditions are considered between bed particles and particles mass flow. Longer lines would need higher number of units, increasing the pressure drop and the compressor work, which is illustrated by the reduction of *P* parameter, Fig. 11-c. An optimum performance is shown for case C when sand particles and airflow reach 535 ºC at L_{unit} = 225 m.

An example of the steady state temperature profiles for case B with $w_{rec} = 0.5\ m$ and L_{unit} = 350 m is shown in Fig. 12. The high inlet temperature to the LPSR is obtained due to the compressor effect (T_1 in Fig. 1). After that, the temperatures of the glass covers and the bed increase up to the thermal equilibrium. The low pressure conditions set between both covers reduce the thermal losses, ensuring high bed temperatures.

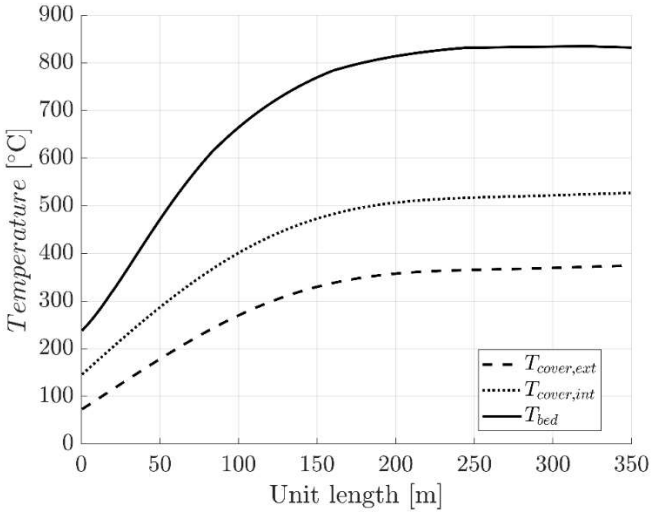

Figure 12. Temperature profiles for BDLFR and LPSR designs characterized by $w_{rec} = 0.5\ m$, ***e*** = 0.8 and L_{line} = 350 m.

Figure 13 shows the results for $w_{rec} = 1\ m$ and $Q''_{BD} = 7.62\ kW/m^2$. The lower average heat flux reduces the bed temperature up to T_{bed} = 630 ºC for cases A and B. The optimum length is shorter (Fig. 13-b/c), showing also lower temperatures than for w_{rec} = 0.5 m. However, as the receiver is wider than in Fig. 11, higher mass flows of air and sand are heated up. Due to that, *P* values shown in Fig. 13-c are slightly higher than for w_{rec} = 0.5 m although the temperature is lower.

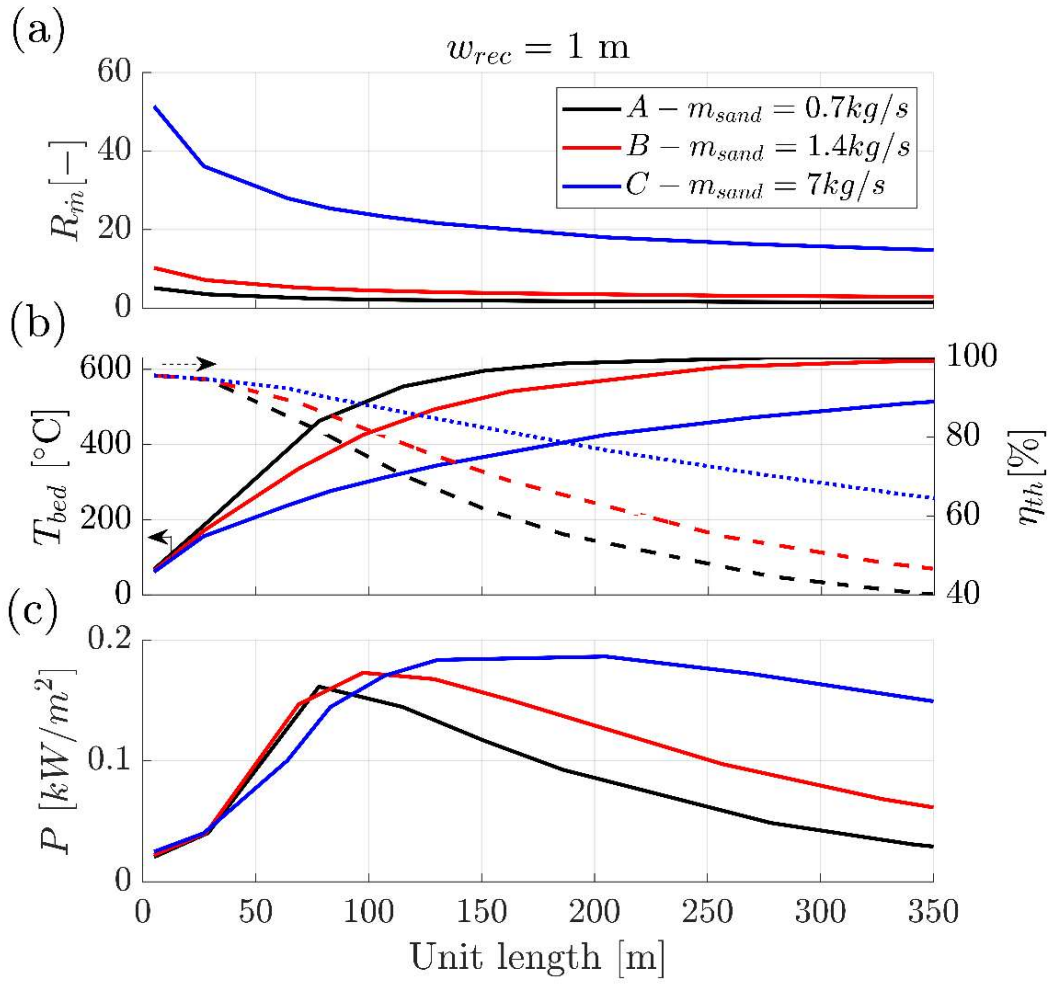

Figure 13. LPSR performance for $w_{rec} = 1\ m$: (a) sand to air mass flow ratio, (b) bed temperature and thermal efficiencies, (c) performance parameter.

The comparison between both receiver widths is carried out fixing different bed temperatures and employing Figs. 11 and 13. Table 4 shows the results for several bed temperatures, which values vary depending on the industrial application. Temperatures from 200 to 400 ºC may be integrated for process heat on industry. Higher temperatures of 600 ºC and 800 ºC may be pursued for Rankine CSP plants and sCO_2 cycles, respectively. Once this bed temperature is fixed, the mass flow percentage is selected for each receiver width. This value is chosen for the maximum *P* value (Figs. 11-c and 13-c) as it would ensure the maximum performance for such bed temperature, which would reduce the aperture area of heliostats. In this way, the line length is obtained. Fig. 11 shows an example of this procedure for a target temperature of 400 ºC.

Table 4. Comparison of the LPSR performance for different bed temperatures. Bold letters indicate the best configuration for each target temperature.

	T_{bed} = 200 ºC		T_{bed} = 400 ºC		T_{bed} = 600 ºC		T_{bed} = 800 ºC	
	w_{rec} [m]		w_{rec} [m]		w_{rec} [m]		w_{rec} [m]	
	0.5	**1**	0.5	**1**	**0.5**	1	**0.5**	1
w_{hyp} [m]	3.3	**3.3**	3.3	**3.3**	**3.3**	3.3	**3.3**	3.3
Case [-]	C	**C**	C	**C**	**C**	A	**B**	-
$\dot{m}_{sand}$ [kg/s]	1.75	**7**	1.75	**7**	**1.75**	0.7	**0.35**	-
L_{line} [m]	75	**48**	154	**180**	**280**	156	**245**	-
$N_{lines} = \frac{\max(\dot{m}_{sand})}{\dot{m}_{sand,i}}$ [-]	4	**1**	4	**1**	**1**	2.5	**1**	-
A_{SF} [$10^3 \cdot m^2$]	5.33	**0.85**	10.94	**3.19**	**4.97**	6.92	**4.35**	-

The influence of the sand mass flow is studied comparing between receiver widths for a fixed bed temperature. Therefore, the number of lines needed to reach the maximum sand mass flow at a fixed bed temperature is calculated dividing the maximum sand mass flow by the sand mass flow of each configuration, which determines the number of lines needed (N_{lines}) and the total aperture area.

The results of Table 4 show that the bed temperature establishes the best LPSR configuration. The target temperature of $T_{bed} = 200\ ºC$ needs a receiver of $w_{rec} = 1\ m$ with line length of $L_{line} = 48\ m$ for a sand mass flow of $\dot{m}_{sand} = 7\ kg/s$. This configuration maximizes the performance value, which reduces the aperture area.

For a temperature of $T_{bed} = 400\ ºC$, the configuration that reduces the heliostats area while maximizing the heat absorbed by air and particles presents a width of $w_{rec} = 1\ m$, which results in a line length of $L_{line} = 180\ m$. A narrower receiver ($w_{rec} = 0.5\ m$) would need $N_{lines} = 4$ to obtain the same sand mass flow.

In contrast, the increase of the bed temperature up to $T_{bed} = 600\ ºC$ reveals that the best configuration is shown for $w_{rec} = 0.5\ m$ and case C as it reduces the total length. This result is a consequence of the *P* value, which is near maximum at that configuration for a bed temperature of 600 ºC, Fig. 11-c. Higher bed temperatures present limitations on the receiver width, as the average flux intensity is not high enough to reach the target temperature. In this way, the bed temperatures of $T_{bed} = 800\ ºC$ presents an optimum receiver width of $w_{rec} = 0.5\ m$.

5. Conclusions

This paper explores the performance of a new CST that employs particles and air as HTF at high temperature. This technology is based on a new linear-beam down solar field that redirects linearly the energy on a new linear particle solar receiver. The novelty of the approach avoids the construction of a solar tower placing the receiver at the ground level. Therefore, a primary linear Fresnel field of heliostats is coupled with a secondary linear beam-down reflector. The design of the linear particle solar receiver allows the horizontal

movement of particles due to the fluid-like behavior of the fluidized air and the particles mixture.

To simplify the optic analysis, the linear beam-down solar field is based on Fresdemo design, considering fixed its main dimensions, such as the positions of primary heliostats and the height of the absorber tube, where the focus of the secondary beam-down reflector is set. The coupled influence of the eccentricity and the receiver width on the average flux intensity has been studied. The comparison of flat and curved primary reflectors show that the flat option can be neglected due to the low average intensity flux obtained on the ground receiver.

When employing curved primary mirrors, the sharper the hyperbola of the secondary reflector, the lower incident power on the receiver. Thus, low eccentricity secondary reflectors show the highest incident powers on the linear particle solar receiver, with values of 19.6 kW/m^2, but with low solar field efficiency of 13.6% for a narrow receiver width of 0.1 m. Such a high concentration is achieved due to the minimization of the spillage error. The increase of the receiver width and the eccentricity shows higher solar field efficiencies due to the reduction of the hyperbola width, which decreases the shadow on the primary reflectors. However, it presents the drawback of decreasing the average flux intensity up to 11.49 kW/m^2 and 7.61 kW/m^2 for receiver widths of 0.5 m and 1 m, respectively, at noon.

The performance of this new particle receiver has been studied for different widths, lengths and sand mass flows fixing the bed temperature. Target bed temperatures of 200 ºC, 400 ºC, 600 ºC and 800 ºC have been considered simulating the integration of CST with medium and high temperature process heat, Rankine CSP and sCO_2, respectively. The results illustrate how to optimize each design maximizing the heat gained by air and particles mass flows. The summary of the results shows line lengths, receiver widths and sand mass flow of:

- At 200 ºC: $L_{line} = 48\ m$, $w_{rec} = 1\ m$ and $\dot{m}_{sand} = 7\ kg/s$;
- At 400 ºC: $L_{line} = 180\ m$, $w_{rec} = 1\ m$ and $\dot{m}_{sand} = 7\ kg/s$;
- At 600 ºC: $L_{line} = 280\ m$, $w_{rec} = 0.5\ m$ and $\dot{m}_{sand} = 1.75\ kg/s$;
- At 800 ºC: $L_{line} = 245\ m$, $w_{rec} = 0.5\ m$ and $\dot{m}_{sand} = 0.35\ kg/s$.

Therefore, the configuration of both the optic system and the particle receiver should be analyzed for each industrial process. Furthermore, even though the solar field employed was not designed nor optimized for a linear beam-down approach, the results demonstrate the feasibility of this new CST approach by its promising results.

Further works will design and test a lab-scale prototype to analyze the horizontal mass flow of particles. In this sense, the design of the gas distributor and the openings between beds will play a significant role on the residence time distribution of particles on each bed, and thus, on the solar receiver performance.

Acknowledgements

This work has been supported by the Spanish Government under the project ENE2015-69486-R (MINECO/FEDER, UE), by “Comunidad de Madrid” and European Structural Funds under the project ACES2030-CM project (S2018/EMT-4319) and by the fellowship “Ayuda a la investigación en energía y medio ambiente” of Fundación Iberdrola España.

Appendix A. Supplementary material

Supplementary video associated with the linear particle solar receiver design can be found attached to this submission.

Appendix B. Fluidized bed model

From (Briongos et al., 2018):

- Emulsion phase:
  Solid phase:

$$Q'''_{net} = (1-a_B)(1-\varepsilon_e)k_e\frac{\partial^2 T_s}{\partial z^2} + (1-a_B)(1-\varepsilon_e)k_r\frac{\partial^2 T_s}{\partial z^2} + Q'''_{gs} + Q'''_{bbs} + Q'''_{sand} + Q'''_{conv,loss} \quad \text{Eq. (B.1)}$$

  Gas phase:

$$Q'''_{gs} = U_{ge}\rho_{ge}c_{pge}\frac{\partial T_{ge}}{\partial z} \quad \text{Eq. (B.2)}$$

- Bubble phase:

$$Q'''_{bbs} = U_b\rho_{gb}c_{pgb}\frac{\partial T_{gb}}{\partial z} \quad \text{Eq. (B.3)}$$

where *z* represents the vertical direction of the bed, $Q'''_{conv,loss}$ considers the heat losses to the surroundings due to convection, which are assumed as the 5% of the incoming irradiation per unit of bed surface (Q''_{BD}), Q'''_{sand} represents the heat transferred by the mass flow of particles:

$$Q'''_{sand} = \dot{m}'''_{sand}c_{p,sand}(T_s - T_{s,in}) \quad \text{Eq. (B.4)}$$

where $\dot{m}'''_{sand}$ is the mass flow of particles per unit of bed volume.

$T_{s,in}$ is the particles temperature at the inlet, which matches the bed temperature of the previous unit. Q'''_{net} refers to the energy balance on the bed surface considering the incoming concentrated irradiation, the convection heat losses and the radiative heat losses.

$$Q'''_{net} = \left(\alpha_{bed}Q''_{in}\frac{A_{bed}}{A_{p,sL}}\right)a_p - (Q'''_{air,out} + Q'''_{r,out}) \quad \text{Eq. (B.5)}$$

where Q''_{in} is the heat flux received from the LBD after considering the transmissivity of the glass covers, $A_{p,sL}$ is the effective heat transfer area at the top bed considering all fluidized particles. The effective bed absorptivity, α_{bed}, depends on the particle emissivity and the fluidization conditions, as shown in (Mazza et al., 1991). $Q_{air,out}$ considers the energy gained by the fluidizing air through the bed:

$$Q_{air,out} = \dot{m}_{air}c_{p,air}(T_{air,out} - T_{air,in}) \quad \text{Eq. (B.6)}$$

and $Q'''_{r,out}$ is the radiative heat loss from the bed surface:

$$Q'''_{r,out} = \varepsilon_{eff}\sigma F_{ij} a_p (T_s^4 - T_{cover}^4) \qquad \text{Eq. (B.7)}$$

659

660 **References**

661 Abbas, R., Martínez-Val, J.M., 2017. A comprehensive optical characterization of linear
662 Fresnel collectors by means of an analytic study. Appl. Energy 185, 1136–1151.
663 https://doi.org/10.1016/j.apenergy.2016.01.065

664 Abbas, R., Montes, M.J., Piera, M., Martínez-val, J.M., 2012. Solar radiation concentration
665 features in Linear Fresnel Reflector arrays. Energy Convers. Manag. 54, 133–144.
666 https://doi.org/10.1016/j.enconman.2011.10.010

667 Almendros-ibáñez, J.A., Fernández-torrijos, M., Díaz-heras, M., Belmonte, J.F., Sobrino,
668 C., 2018. A review of solar thermal energy storage in beds of particles: Packed and fl
669 uidized beds. Sol. Energy 0–1. https://doi.org/10.1016/j.solener.2018.05.047

670 Bhattacharya, B., Sathiyamoorthy, D., Govardhana Rao, V., Mahajan, S. P., 1999. Solid
671 circulation in a compartmented gas fluidized bed, Powder Technol., 101, 3, 191-204

672 Benoit, H., Pérez López, I., Gauthier, D., Sans, J.L., Flamant, G., 2015. On-sun
673 demonstration of a 750 °C heat transfer fluid for concentrating solar systems: Dense
674 particle suspension in tube. Sol. Energy 118, 622–633.
675 https://doi.org/10.1016/j.solener.2015.06.007

676 Bernhard, R., Laabs, H., Lalaing, J. De, 2008. Linear Fresnel collector demonstration on
677 the PSA, Part I–design, construction and quality control, in: SolarPACES.

678 Briongos, J. V., Gómez-Hernández, J., González-Gómez, P.A., Serrano, D., 2018. Two-
679 phase heat transfer model of a beam-down gas-solid fl uidized bed solar particle
680 receiver. Sol. Energy 171, 740–750. https://doi.org/10.1016/j.solener.2018.07.016

681 Buie, D., Monger, A.G., Dey, C.J., 2003. Sunshape distributions for terrestrial solar
682 simulations. Sol. Energy 74, 113–122. https://doi.org/10.1016/S0038-092X(03)00125-
683 7

684 Calderón, A., Palacios, A., Barreneche, C., Segarra, M., Prieto, C., Rodriguez-Sanchez,
685 A., Fernández, A.I., 2018. High temperature systems using solid particles as TES and
686 HTF material: A review. Appl. Energy 213, 100–111.
687 https://doi.org/10.1016/j.apenergy.2017.12.107

688 Calvet, N., Martins, M., Grange, B., Perez, V.G., Belasri, D., Ali, M.T., Armstrong, P.R.,
689 2016. The Masdar Institute Solar Platform: A new research facility in the UAE for
690 development of CSP components and thermal energy storage systems. AIP Conf.
691 Proc. 1734. https://doi.org/10.1063/1.4949191

692 Chacartegui, R., Alovisio, A., Ortiz, C., Valverde, J.M., Verda, V., Becerra, J.A., 2016.
693 Thermochemical energy storage of concentrated solar power by integration of the
694 calcium looping process and a CO2 power cycle. Appl. Energy 173, 589–605.
695 https://doi.org/10.1016/j.apenergy.2016.04.053

696 Chirone, R., Salatino, P., Ammendola, P., Solimene, R., Magaldi, M., Sorrenti, R., De
697 Michele, G., Donatini, F., 2017. Development of a Novel Concept of Solar
698 Receiver/Thermal Energy Storage System Based on Compartmented Dense Gas

699 Fluidized Beds. AIP Conf. Proc. 1850. https://doi.org/10.1063/1.4984447

700 Chong, Y.O., Nicklin, D.J., Tait, P.J., 1986. Solids exchange between adjacent fluid beds
701 without gas mixing. Powder Technol. 47, 151–156. https://doi.org/10.1016/0032-
702 5910(86)80111-5

703 Davidson, J. F., Harrison, D., 1963. Fluidised Particles, first ed. Cambridge University
704 Press, Great Britain.

705 Davidson, J. F., Clift, R., Harrison, D., 1985. Fluidization, second ed. Academic Press Inc.,
706 Orlando, Florida, pp. 32887.

707 Diago, M., Crespo Iniesta, A., Soum-Glaude, A., Calvet, N., 2018. Characterization of
708 desert sand to be used as a high-temperature thermal energy storage medium in
709 particle solar receiver technology, Applied Energy, 216, 402-413.

710 Duffie, J. a., Beckman, W. a., Worek, W.M., 2003. Solar Engineering of Thermal
711 Processes, 4nd ed., Journal of Solar Energy Engineering.
712 https://doi.org/10.1115/1.2930068

713 Ebert, M., Amsbeck, L., Rheinländer, J., Schlögl-, B., Schmitz, S., Sibum, M., Uhlig, R.,
714 Buck, R., 2018. Operational Experience of a Centrifugal Particle Receiver Prototype,
715 in: SolarPACES 2018.

716 Ermanoski, I., Siegel, N.P., Stechel, E.B., 2013. A New Reactor Concept for Efficient
717 Solar-Thermochemical Fuel Production. J. Sol. Energy Eng. 135, 031002.
718 https://doi.org/10.1115/1.4023356

719 Fang, M., Yu, C., Shi, Z., Wang, Q., Luo, Z., Cen, K., 2003. Experimental research on solid
720 circulation in a twin fluidized bed system. Chem. Eng. J. 94, 171–178.
721 https://doi.org/10.1016/S1385-8947(03)00058-5

722 Fernández-Torrijos, M., Albrecht, K.J., Ho, C.K., 2018. Dynamic modeling of a
723 particle/supercritical CO2 heat exchanger for transient analysis and control. Appl.
724 Energy 226, 595–606. https://doi.org/10.1016/j.apenergy.2018.06.016

725 Formisani, B., Girimonte, R., Mancuso, L., Cosenza, R., 1998. Analysis of the fluidization
726 process of particle beds at high temperature. Chem. Eng. S 53, 951–961.

727 Geng, S., Qian, Y., Zhan, J., Zhang, H., Xu, G., Liu, X., 2017. Prediction of solids
728 residence time distribution in cross- flow bubbling fluidized bed. Powder Technol. 320,
729 555–564. https://doi.org/10.1016/j.powtec.2017.07.085

730 Gokon, N., Izawa, T., Abe, T., Kodama, T., 2014. Steam gasification of coal cokes in an
731 internally circulating fluidized bed of thermal storage material for solar
732 thermochemical processes. Int. J. Hydrogen Energy 39, 11082–11093.
733 https://doi.org/10.1016/j.ijhydene.2014.05.124

734 Gokon, N., Takahashi, S., Yamamoto, H., Kodama, T., 2008. Thermochemical two-step
735 water-splitting reactor with internally circulating fluidized bed for thermal reduction of
736 ferrite particles. Int. J. Hydrogen Energy 33, 2189–2199.
737 https://doi.org/10.1016/j.ijhydene.2008.02.044

738 Gómez-Hernández, J., González-Gómez, P.Á., Ni-song, T., Briongos, V., Santana, D.,
739 2017. Design of a Solar Linear Particle Receiver Placed at the Ground Level, in: AIP
740 Conference Proceedings. American Institute of Physics, p. 2033.

741 https://doi.org/10.1063/1.5067169

742 González, D.F., Ruiz-Bustinza, I., Piñuela, J., Verdeja, L.F., Fernández-González, D.,
743 Ruiz-Bustinza, Í., González-Gasca, C., Noval, J.P., Mochón-Castaños, J., Sancho-
744 Gorostiaga, J., 2018. Concentrated solar energy applications in materials science and
745 metallurgy. Sol. Energy 170, 520–540. https://doi.org/10.1016/j.solener.2018.05.065

746 Ho, C., Peacock, G., Albrecht, K., Yellowhair, J., Ray, D., 2018. On-Sun Testing of a 1
747 MWt Particle Receiver with Automated Particle Mass-Flow and Temperature Control,
748 in: SolarPACES2018.

749 Ho, C.K., 2016. A review of high-temperature particle receivers for concentrating solar
750 power. Appl. Therm. Eng. 109, 958–969.
751 https://doi.org/10.1016/j.applthermaleng.2016.04.103

752 Ho, C.K., Christian, J., Yellowhair, J., Jeter, S., Golob, M., Nguyen, C., Repole, K., Abdel-
753 Khalik, S., Siegel, N., Al-Ansary, H., El-Leathy, A., Gobereit, B., 2017. Highlights of
754 the high-temperature falling particle receiver project: 2012 - 2016. AIP Conf. Proc.
755 1850, 2012–2016. https://doi.org/10.1063/1.4984370

756 Ho, C.K., Christian, J.M., E. Yellowhair, J., Armijo, K., Kolb, W.J., Jeter, S., Golob, M.,
757 Nguyen, C., 2018. On-Sun Performance Evaluation of Alternative High-Temperature
758 Falling Particle Receiver Designs. J. Sol. Energy Eng. 141, 011009.
759 https://doi.org/10.1115/1.4041100

760 Ho, C.K., Iverson, B.D., 2014. Review of high-temperature central receiver designs for
761 concentrating solar power. Renew. Sustain. Energy Rev. 29, 835–846.
762 https://doi.org/10.1016/j.rser.2013.08.099

763 Hua, L., Zhao, H., Li, J., Zhu, Q., Wang, J., 2019. Solid residence time distribution in a
764 cross-flow dense fluidized bed with baffles. Chemical Eng. Science, 200, 320–335

765 Iniesta, A.C., Diago, M., Delclos, T., Falcoz, Q., Shamim, T., Calvet, N., 2015. Gravity-fed
766 Combined Solar Receiver/Storage System Using Sand Particles as Heat Collector,
767 Heat Transfer and Thermal Energy Storage Media. Energy Procedia 69, 802–811.
768 https://doi.org/10.1016/j.egypro.2015.03.089

769 IRENA, 2017. Renewable Power Generation Costs in 2017, SpringerReference.
770 https://doi.org/10.1007/SpringerReference_7300

771 Kincaid, N., Mungas, G., Kramer, N., Zhu, G., 2019. Sensitivity analysis on optical
772 performance of a novel linear Fresnel concentrating solar power collector. Sol.
773 Energy 180, 383–390. https://doi.org/10.1016/j.solener.2019.01.054

774 Kodama, T., Bellan, S., Gokon, N., Seok, H., 2017. Particle reactors for solar
775 thermochemical processes. Sol. Energy 156, 113–132.
776 https://doi.org/10.1016/j.solener.2017.05.084

777 Kodama, T., Gokon, N., Cho, H.S., Matsubara, K., Etori, T., Takeuchi, A., Yokota, S.N.,
778 Ito, S., 2016. Particles fluidized bed receiver/reactor with a beam-down solar
779 concentrating optics: 30-kWthperformance test using a big sun-simulator. AIP Conf.
780 Proc. 1734. https://doi.org/10.1063/1.4949206

781 Kodama, T., Gokon, N., Matsubara, K., Yoshida, K., Koikari, S., Nagase, Y., 2014. Flux
782 measurement of a new beam-down solar concentrating system in Miyazaki for
783 demonstration of thermochemical water splitting reactors. Energy Procedia 49, 1990–

784 1998. https://doi.org/10.1016/j.egypro.2014.03.211

785 Kong, W., Wang, B., Baeyens, J., Li, S., Ke, H., Tan, T., Zhang, H., 2018. Solids mixing in
786 a shallow cross-flow bubbling fluidized bed. Chem. Eng. Sci., 187, 213-222

787 Korzynietz, R., Brioso, J.A., Río, A., Quero, M., Gallas, M., Uhlig, R., Ebert, M., Buck, R.,
788 Teraji, D., 2016. Solugas – Comprehensive analysis of the solar hybrid Brayton plant.
789 Sol. Energy 135, 578–589. https://doi.org/10.1016/j.solener.2016.06.020

790 Kunii, D., Levenspiel, O., 1991. Fluidization Engineering.

791 Kuramoto, M., Furusawa, T., Kunii, D., 1985. Development of a New System for
792 Circulating Fluidized Particles within a Single Vessel, Powder Technology, 44, 77 –
793 84.

794 Kuramoto, M., Kunii, D., Furusawa, T., 1986. Flow of Dense Fluidized Particles through an
795 Opening in a Circulation System. Powder Technology, 47, 141 - 149

796 Magaldi, n.d. STEM® - Solar Thermo-Electric Magaldi [WWW Document]. URL
797 https://www.magaldi.com/en/products-solutions/csp-concentrating-solar-power
798 (accessed 5.27.19).

799 Marugán-Cruz, C., Serrano, D., Gómez-Hernández, J., Sánchez-Delgado, S., 2018. Solar
800 multiple optimization of a DSG linear Fresnel power plant. Energy Convers. Manag.

801 Mazza, G.D., Berto, C.A., Barreto, G.F., 1991. Evaluation media of radiative heat transfer
802 properties in dense particulate. Powder Technol. 67, 137–144.

803 Mehos, M., Turchi, C., Vidal, J., Wagner, M., Ma, Z., Ho, C., Kolb, W., Andraka, C., 2017.
804 Concentrating Solar Power Gen3 Demonstration Roadmap. Nrel/Tp-5500-67464 1–
805 140. https://doi.org/10.2172/1338899

806 Mekhilef, S., Saidur, R., Safari, A., 2011. A review on solar energy use in industries.
807 Renew. Sustain. Energy Rev. 15, 1777–1790.
808 https://doi.org/10.1016/j.rser.2010.12.018

809 Mori, S., Wen, C.Y., 1975. Estimation of bubble diameter in gaseous fluidized beds. AIChE
810 J. 21, 109–115. https://doi.org/10.1002/aic.690210114

811 Mujumdar, A. S., (2014). Handbook of industrial drying, CRC Press

812 Ortiz, C., Chacartegui, R., Valverde, J.M., Alovisio, A., Becerra, J.A., 2017. Power cycles
813 integration in concentrated solar power plants with energy storage based on calcium
814 looping. Energy Convers. Manag. https://doi.org/10.1016/j.enconman.2017.03.029

815 Puerto Errado 2 Thermosolar Power Plant [WWW Document], n.d. URL
816 https://solarpaces.nrel.gov/puerto-errado-2-thermosolar-power-plant (accessed
817 11.27.18).

818 Sánchez-González, A., Gómez-Hernández, J., 2020. Beam-down linear Fresnel reflector:
819 BDLFR. Renew. Energy 146, 802–815. https://doi.org/10.1016/j.renene.2019.07.017

820 Santana, D., Gómez-Hernández, J., Villa Briongos, J., González-Gómez, P.Á., 2017.
821 Sistema óptico de haz descendente lineal solar. ES 2648148 A1.

822 Segal, A., Epstein, M., 2001. The optics of the solar tower reflector. Sol. Energy 69, 229–
823 241. https://doi.org/10.1016/S0038-092X(00)00137-7

824 Stein, W.H., Buck, R., 2017. Advanced power cycles for concentrated solar power. Sol.
825 Energy 152, 91–105. https://doi.org/10.1016/j.solener.2017.04.054

826 Tregambi, C., Salatino, P., Solimene, R., Montagnaro, F., 2018. An experimental
827 characterization of Calcium Looping integrated with concentrated solar power. Chem.
828 Eng. J. 331, 794–802. https://doi.org/10.1016/j.cej.2017.08.068

829 Vant-Hull, L., 2014. Issues with beam-down concepts. Energy Procedia 49, 257–264.
830 https://doi.org/10.1016/j.egypro.2014.03.028

831 Vasquez, R., Demirkaya, G., Goswami, D.Y., Stefanakos, E., Rahman, M.M., 2011. Heat
832 transfer analysis of parabolic trough solar receiver. Appl. Energy 88, 5097–5110.
833 https://doi.org/10.1016/j.apenergy.2011.07.012

834 Wendelin, T., 2003. Soltrace: a New Optical Modeling Tool for Concentrating Solar Optics,
835 in: International Solar Energy Conference.

836 Wendelin, T., Dobos, A., Lewandowski, A., 2013. SolTrace: A New Optical Modeling Tool
837 for Concentrating Solar Optics, NREL, National Renewable Energy Laboratory.
838 https://doi.org/10.1115/ISEC2003-44090

839 Wu, W., Amsbeck, L., Buck, R., Uhlig, R., Ritz-paal, R., 2014. Proof of concept test of a
840 centrifugal particle receiver. Energy Procedia 49, 560–568.
841 https://doi.org/10.1016/j.egypro.2014.03.060

842 Xiao, G., Guo, K., Luo, Z., Ni, M., Zhang, Y., Wang, C., 2014. Simulation and experimental
843 study on a spiral solid particle solar receiver. Appl. Energy 113, 178–188.
844 https://doi.org/10.1016/j.apenergy.2013.06.045

845 Yadav, D., Banerjee, R., 2016. A review of solar thermochemical processes. Renew.
846 Sustain. Energy Rev. 54, 497–532. https://doi.org/10.1016/j.rser.2015.10.026

847 Zhu, G., Lewandowski, A., 2012. A New Optical Evaluation Approach for Parabolic Trough
848 Collectors: First-Principle OPTical Intercept Calculation. J. Sol. Energy Eng. 134,
849 041005. https://doi.org/10.1115/1.4006963

850